H.S.

DESIGN OF A HIGH INTENSITY ELECTRON GUN AND ITS FOCUSING SYSTEM

Henrik Stenlund

CONTENTS

ABSTRACT

An electron gun and a beam transport system suitable for x-ray excitation of gaseous samples has been designed. It is intended to serve as an x-ray source for a grating spectrometer below 1 keV energies.

The constraints put on the size and position of the source by the spectrometer slit system at given resolution are studied. Then the minimal beam radius limited by space charge is calculated, and the basic design parameters are fixed.

The electron gun is of Pierce type with a perveance of $P = 3 \times 10^{-7}$ and converging angle of 13°. The electron acceleration voltage is variable between 5 and 10 kV and the maximum output current is 0.3 A. The calculated minimum beam radii (defined to include 95 % of the electrons of the beam) are 0.73 and 0.59 mm for 5 and 10 kV respectively.

The gun shoots the electrons into a three stage beam transport system, which facilitates efficient differential pumping making possible to maintain the pressures of the electron gun and sample cell at 0.1 mPa and 1 kPa respectively in a windowless container. The transport system consists of three magnetic ironless lenses two of which have unit magnifications imaging the gun focus into narrow channels between successive pumping stages. The third stage finally compresses the beam in a linear ratio of 0.429 into the sample gas chamber.

1. INTRODUCTION

Measurement of x-ray emission spectra from gases and vapors is difficult especially in ultrasoft region. Low density as compared to solids and liquids leads unavoidably to low emission intensities. Below about 1 keV energy, where grazing incidence grating spectrometers can give higher resolution than crystal spectrometers, bright and narrow sources are needed. Regular photon sources have moderate brightness but the beam is strongly divergent. Exciting by an electron beam of high brightness can be obtained, but a windowless system is a prerequisite. Thus we are faced with the problem of gas confinement.

Comparing the results from the systems built elsewhere [1-8] we decided to use electron excitation. In this paper we describe the theory of the electron optical system needed for the purpose and finally design the whole excitation gun, which at the present is being made in the laboratory.

Fig. 1.1. depicts the excitation gun. An electron beam (5-10 keV) ejected from a Pierce-type electron gun is focused by magnetic lenses two times into narrow channels to facilitate differential pumping and the third time into the sample gas cell itself. This arrangement allows to maintain a gas pressure of 1 kPa in the sample while the electron gun stage works at 0.1 mPa, a pressure low enough for reasonable lifetime of a hot cathode. The design of the vacuum pumping system is not dealt here.

Magnetic lenses are realized by three identical ironless coils: two of them have unit magnification whereas the third compresses the electron beam entering the sample gas chamber. The perveance

$$P = I/V^{3/2},$$ (1.1)

where I is the beam current and V the accelerating anode voltage, has been selected moderate to obtain a fairly narrow beam, which can be focused easily and still get out reasonable x-ray intensity. The conservative value of P saves us also from involved computer calculations and experiments with electrolytic tanks, which are necessary in the design of very high perveance guns.

In section 2.1. we represent the theory of space charge limited electron beam and calculate spreading as well as the optimum value of linear compression. Section 2.2. deals with the requirements set by the slit system of the spectrometer.

Chapter 3 is devoted to study the theory and design of the electron gun. Sections 3.1.-3.6. describe how to obtain the parameters of the gun and section 3.7. describes the effects of thermal velocities of the electrons.

In chapter 4. we investigate the appropriate focusing system by calculating the field of a coil, section 4.1., and the focal length, sections 4.2. and 4.3. whereas in section 4.4. we put together all the information obtained from the focusing system. Chapter 5. discusses the results obtained in this work.
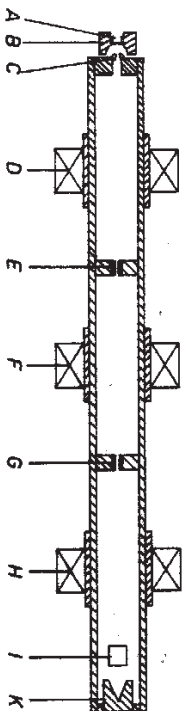
Figure 1.1. The beam transport system. A = cathode of the electron gun, B = focusing electrode, C = anode aperture, D = first focusing coil, E = first orifice for differential pumping, F = second focusing coil, G = second orifice, H = third focusing coil, I = sample gas chamber, K = Faraday cup.

2. CONSTRAINTS FOR THE BEAM

In this chapter we solve the behaviour of an electron beam with space charge in field-free region. We calculate the place and the radius of the converging cylindrical beams of known perveance. We also study the spectrometer slit system to see how far from the entrance slit we can place the radiation source without too large intensity losses.

2.1. Limitations caused by space charge

Due to the repulsive Coulomb force a dense electron beam spreads out rapidly while travelling in field-free space. Therefore also a beam initially travelling towards the tip of a cone spreads out so that the beam edge departs from the cone surface and the beam minimum moves away from the apex of the cone. In the following we are going to calculate the place and the radius of the minimum of a cylindrical beam.

The equation of motion given by Pierce [9] for the beam electrons is

$$r''(z) = \frac{I\sqrt{\frac{m}{e}}}{4\sqrt{2}\,\epsilon_0\, V^{3/2} r\,\pi} = \frac{\alpha^2}{2}\cdot\frac{1}{r}. \qquad (2.1)$$

By changing the variables to

$$R = r/r_a, \quad R_a = 1 \qquad (2.2)$$

$$z = \alpha z/r_a \qquad (2.3)$$

we obtain $(R' = \partial R/\partial Z)$

$$R'' = 1/2R. \qquad (2.4)$$

This can be integrated once

$$(R')^2 = \ln R + (R'_a)^2. \qquad (2.5)$$

Since at the minimum $R' = 0$, Eq. (2.5) yields for minimum radius

$$r_m = r_a \exp\left[-(\lambda/a)^2\right] = \kappa\, r_a . \qquad (2.6)$$

Here $-\lambda$ is the slope of the beam edge at the initial point and κ is the beam compression ratio. Integrating (2.5) further we obtain

$$z = \frac{2r_a}{a}\, e^{-(\lambda/a)^2} \int_{\frac{\pm\sqrt{\ln R + (R'/R_a)^2}}{R_a}} e^{u^2}\, du . \qquad (2.7)$$

The distance of the beam minimum is

$$z_m = \frac{2r_a}{a}\, e^{-(\lambda/a)^2} \int_0^{\lambda/a} e^{u^2}\, du = \frac{2\kappa r_a}{a} \int_0^{\sqrt{-\ln\kappa}} e^{u^2}\, du . \qquad (2.8)$$

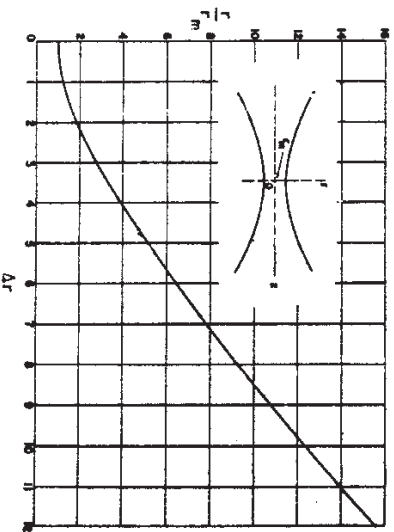This integral can be calculated numerically. Eq. (2.7) is shown graphically in Fig. 2.1.

Figure 2.1. Beam spreading caused by space charge [10].

Here

$$\Delta r = az/r_m , \qquad a = 174.1/\sqrt{P} . \qquad (2.9)$$

As will become apparent in the next section small diameter sources are advantageous and thus we examine beams with smallest possible diameter. Since the beam is symmetrical in both directions in field-free regions, the minimum must be situated in the center of the volume to be examined. We should determine what kind of a beam of definite perveance will flow through a region of known length h and width δ (a cylindrical tube). This describes the situation when the beam crosses the sample gas chamber and emits radiation from the same volume into the spectrometer. To exhibit the fact that δ as a function of κ has a minimum (h and P fixed) we have drawn curves (Appendix A) which are derived graphically from Fig. 2.1.

To calculate accurately the minimum of $\delta(\kappa)$ we keep z_m and a constant and differentiate Eq. 2.8. to obtain ($\frac{d\delta}{d\kappa} = 0$ at the extremum)

$$\left(\frac{d\delta}{d\kappa}\right)\frac{\kappa}{a} \int_0^{\sqrt{-\ln\kappa}} e^{u^2}\, du + \frac{\delta}{a} \int_0^{\sqrt{-\ln\kappa}} e^{u^2}\, du - \frac{\delta e^{-\ln\kappa}}{2a\sqrt{-\ln\kappa}} = 0 . \qquad (2.10)$$

Eq. (2.10) can be turned into the standard form of transcendental equations, which can be solved employing usual numerical methods

$$\frac{1}{\kappa} = 2\sqrt{-\ln\kappa} \int_0^{\sqrt{-\ln\kappa}} e^{u^2}\, du . \qquad (2.11)$$

Eq. (2.11) has two solutions. The first one $\kappa = 0$ is unphysical as the beam can not be compressed into zero diameter. The other solution $\kappa \simeq 0,429$ is evidently quite independent of other parameters of the system and gives a minimum to δ. This means that the respective value

$K_0 = 0,429$ $\sqrt{-\ln K_0} = 0,9199448$ $\int_6^{\sqrt{-\ln K_0}} e^{u^2}\, du = 1,2115313$

of κ is the same for all cylindrical space charge limited beams in field-free regions.

The compression ratio κ for minimum beam entrance diameter through a cylinder has been evaluated by Ivey [11] by using a partly graphical method and his result for $\kappa \approx 0,426$ is in good accordance with the value we obtained.

We have chosen for the gun perveance P to be of the order $0,3 \cdot 10^{-6}$ (to be explained in the chapter on gun design) this being approximately the perveance of the beam. The spectrometer requires the source height to be of order 10 mm (see next section) and thus we can easily calculate the values of δ and r_m to be 0,88 mm and 0,19 mm, respectively. These figures give us some guidelines in choosing the gun parameters, its optical properties and the strength of the focusing coils.

2.2. Requirements of the slit system

To gain the maximum available amount of radiation coming through the entrance slit of the x-ray spectrometer on its concave spherical diffraction grating we must study the effects of the slit system carefully. The radiation is generated in the volume crossed by the electron beam in the sample gas thus exciting the inner shell electrons of the atoms. The shape of the electron beam is determined by space charge (cf. Fig. 2.1.) as is depicted in Fig. 2.2.

The horizontal section of the slit system is shown in Fig. 2.3. The cylindrical source has been replaced by a ribbon source because the calculations become thus much easier. In practice there is a spherical mirror and another slit between the entrance slit and the concave spherical diffraction grating. To a good approximation their effects can be neglected. The ribbon source is a band of length h and width H having constant brightness.
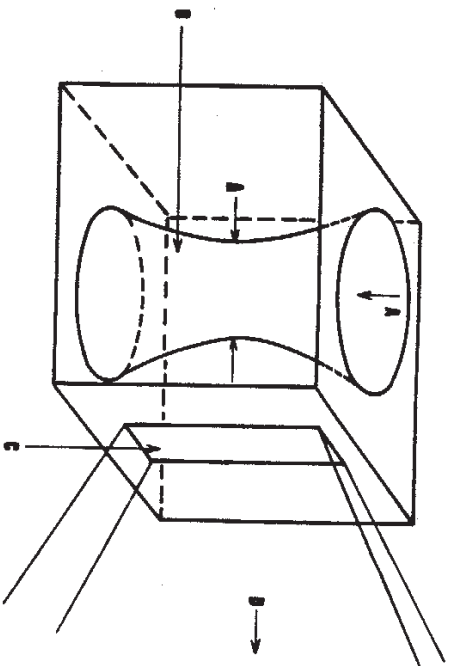
Figure 2.2. The electron beam focused into the sample gas chamber. A is of the order 1 mm. A = entering electron beam, B = radiative volume, C = exit slit, D = radiation to x-ray spectrometer.
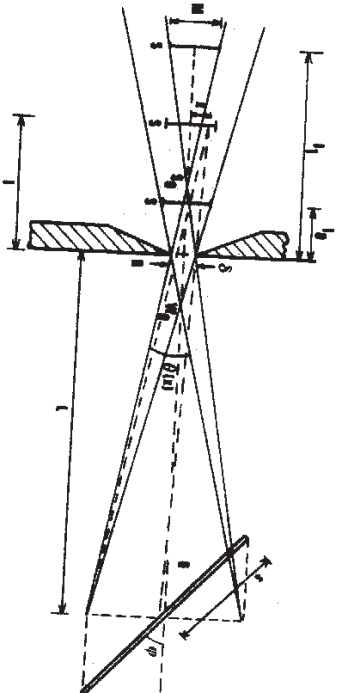

Figure 2.3. The slit system and the ribbon source. S = source, R = slit, G = grating.

The calculations are further simplified by symmetrizing the grating. This is done by taking the projection of the grating to receive the intensity.

The intensity of radiation arriving at the grating from the point x in the source is proportional to the solid angle $\theta(x)$ (a plane angle in Fig. 2.3.) the grating subtends the point of emission. The solid angle can be approximated by the product of two plane angles, $\theta(x)$ shown in Fig. 2.3. and the other in the plane perpendicular to it. This further simplifies the calculations. The length of the ribbon (not shown in Fig. 2.3.) is inessential at this point; we assume it to be large enough to neglect all end effects.

The special points ℓ_0, ℓ_1, S_0 and W_0 are easily calculated according to Fig. 2.3.

$$\ell_0 = \frac{L(M - \delta)}{2s \sin \phi + \delta} \quad , \qquad L \gg M, \ L \gg \delta \ , \tag{2.12}$$

$$S_0 = \frac{\delta L}{2s \sin \phi - \delta} \qquad \ell_0 > S_0 \ , \tag{2.13}$$

$$W_0 = \frac{\delta L}{2s \sin \phi} \ , \tag{2.14}$$

$$\ell_1 = \frac{L(M + \delta)}{2s \sin \phi - \delta} \qquad M > \delta. \tag{2.15}$$

Now we can divide the ℓ-axis into these regions according to their limiting properties:

1. $0 \leq \ell \leq S_0$ The source size does not limit θ.
2. $S_0 \leq \ell \leq \ell_0$ The source size partially limits θ.
3. $\ell_0 \leq \ell \leq \ell_1$ The source size limits θ.
4. $\ell_1 \leq \ell$.   The slit and the source size limit θ.

Next task is to calculate how the intensity varies as the distance ℓ and other parameters are changed. We are working with an electron beam, whose total current remains constant for different sizes of the beam. This means that we must divide the relative intensity with the beam width M to compensate for the variation of emission density

$$I = \frac{1}{M} \int_{source} \theta(x)dx \ . \tag{2.16}$$

From the geometry of Fig. 2.3. we obtain for the intensity in region 1

$$I_1 = \frac{1}{M} \int_{x_1}^{x_2} dx \left[\arctan\left(\frac{x + s \sin \phi}{L + \ell}\right) - \arctan\left(\frac{s \sin \phi + x}{\ell}\right) \right]$$

$$+ \frac{1}{M} \int_0^{x_1} dx \left[\arctan\left(\frac{s \sin \phi - x}{L + \ell}\right) + \arctan\left(\frac{s \sin \phi + x}{\ell}\right) \right] , \tag{2.17}$$

where

$$x_1 = \frac{\delta}{2} - \frac{\ell(s \sin \phi - \delta/2)}{L} \ ; \ x_2 = \frac{(\ell + L)\delta}{2L} + \frac{\ell s \sin \phi}{L} \ . \tag{2.18}$$

After integration and some tedious manipulations we obtain

$$I_1 = I_2 = \frac{1}{M}\left[\left(\frac{\delta}{2} + s\sin\phi\right)\arctan\left(\frac{\delta/2 + s\sin\phi}{L}\right) +\right.$$

$$- (s\sin\phi - \delta/2)\arctan\left(\frac{s\sin\phi - \delta/2}{L}\right) - \frac{L}{2}\ln\left|\frac{L^2 + \left(\frac{\delta}{2} + s\sin\phi\right)^2}{L^2 + (\delta/2 - s\sin\phi)^2}\right|\right]$$

$$= \text{constant},\qquad\qquad (2.19)$$

$$I_3 = \frac{1}{M}\left[\left(\frac{M}{2} + s\sin\phi\right)\arctan\left(\frac{\frac{M}{2} + s\sin\phi}{L+\ell}\right) +\right.$$

$$- \left(\frac{M}{2} - \frac{\delta}{2}\right)\arctan\left(\frac{\frac{M}{2} - \frac{\delta}{2}}{L+\ell}\right) - \left(s\sin\phi - \frac{\delta}{2}\right)\arctan\left(\frac{s\sin\phi - \frac{\delta}{2}}{L}\right) +$$

$$+ \frac{\ell}{2}\ln\left|\frac{1 + \left(\frac{\frac{M}{2} - \frac{\delta}{2}}{L+\ell}\right)^2}{1 + \left(\frac{\frac{M}{2} + s\sin\phi}{L+\ell}\right)^2}\right| - \frac{L}{2}\ln\left|\frac{1 + \left(\frac{\frac{M}{2} + s\sin\phi}{\ell + L}\right)^2}{1 + \left(\frac{s\sin\phi - \frac{\delta}{2}}{L}\right)^2}\right| \qquad (2.20)$$

and for I_4 we have

$$I_4 = \frac{1}{M}\left[-\left(\frac{M}{2} - \frac{\delta}{2}\right)\arctan\left(\frac{\frac{M}{2} - \frac{\delta}{2}}{\ell}\right) + \frac{\ell}{2}\ln\left|\frac{\ell^2 + \left(\frac{\delta}{2} - \frac{M}{2}\right)^2}{\ell^2 + \left(\frac{\delta}{2} + \frac{M}{2}\right)^2}\right| +\right.$$

$$+ \left(\frac{\delta}{2} + \frac{M}{2}\right)\arctan\left(\frac{\frac{\delta}{2} + \frac{M}{2}}{\ell}\right)\right]. \qquad (2.21)$$

To take into account the third dimension we must consider the geometry in Fig. 2.4. Assuming the height of the source is equal to or smaller than the height of the slit, the slit does not limit the angle θ.

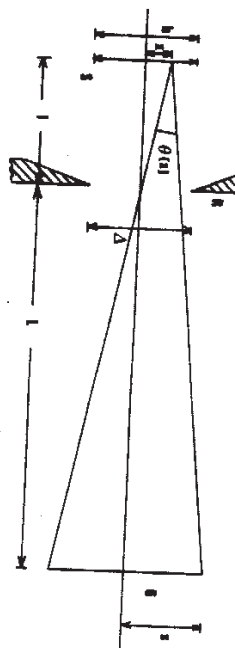We can calculate the corresponding intensity factor I_h as above.

Figure 2.4. The third dimension of the source. S = source, R = slit, G = grating.

We obtain for I_h

$$I_h = 2\arctan\left(\frac{S}{L}\right) \qquad (2.22)$$

and for the relative total intensity

$$I_{tot} = 2\arctan\left(\frac{S}{\ell} + \frac{S}{L}\right)I_i, \qquad i = 1,2,3,4. \qquad (2.23)$$

We can expect that equations (2.19)-(2.21) together with (2.22) give a reasonably good description of the behaviour of real I(ℓ) with a beam shaped as in Fig. (2.2) and therefore the graphs of I(ℓ) have been drawn with practical parameters of the RSM-500 spectrometer (Figs. B.1. and B.2. in Appendix B). The two values of L and φ used are the extreme positions of the grating practical operation taking place between these. As we can see, the intensity remains bounded at large distances (we cannot increase intensity by reducing source size) and all curves with different M have the same asymptote.

At small distances the asymptote bifurcates for each different M and we recognize the advantage of using small diameter sources as the intensity grows faster for small than for large sources.

The effect of moving the grating closer to the slit is the broadening of the high intensity regions as can be seen from equations (2.12) and (2.13). According to Eqs. (2.19)-(2.21) approximately

$$I \sim \delta \qquad (2.24)$$

and thus δ does not essentially influence the determination of the region of maximum intensity.

It seems that for practical beam diameters ($N \approx 0.5 - 1.0$ mm) the distance of the beam from the slit should be of order 40-50 mm to avoid excessive loss of intensity. At 100 mm distance the intensity loss is already 70 %.

3. THEORY OF THE GUN

3.1. The spherical diode

The current between concentric spheres under the influence of space charge has been solved analytically and we can use this information when calculating the characteristics of a high perveance gun with the electrodes formed as spherical sectors placed axially.

In the case of two concentric spheres one of them emitting and the other collecting electrons, Poisson's equation becomes in the presence of space charge ρ

$$\frac{1}{r^2}\frac{d}{dr}\left(r^2\frac{dV}{dr}\right) = \frac{\rho}{\epsilon_0}. \qquad (3.1)$$

If I is the total current and v the velocity of electrons at the distance r from the center of the spheres, we obtain

$$I = 4\pi r^2 \rho v. \qquad (3.2)$$

The energy relation of the electrons is

$$\frac{1}{2}mv^2 = eV, \qquad (3.3)$$

where V equals zero on the surface of the emitter. These equations lead to

$$\frac{d}{dr}\left(r^2\frac{dV}{dr}\right) = \frac{I}{4\pi\epsilon_0}\sqrt{\frac{m}{2eV}}. \qquad (3.4)$$

This equation can not be solved in closed form, but Langmuir and Blodgett [12] have shown an elegant method of series solution in terms of α, a function of r and $\bar{r}_c$, the radius of the emitter

$$\frac{I}{V^{3/2}} = \frac{16\pi\epsilon_0}{9\alpha^2} \cdot \sqrt{\frac{2e}{m}}. \qquad (3.5)$$

Here

$$\alpha = \gamma - 0.3\,\gamma^2 + 0.075\,\gamma^3 - 0.0143182\,\gamma^4 + 0.0021609\,\gamma^5 - 0.0026791\,\gamma^6 + \dots \qquad (3.6)$$

where

$$\gamma = \log\left(\frac{\bar{r}}{\bar{r}_c}\right). \qquad (3.7)$$

Equation (3.5) determines the limiting current of the spherical diode in terms of the potential between the spheres. It is obvious that the current depends only on the ratio of the radii of the spheres. Because the emitter is outside the collector, γ and hence also α are negative. The function $\alpha(\bar{r}_c/r)$ is shown in table 3.1.

Since the electrodes of the actual gun are segments of half angle θ, the current relation becomes

$$\frac{I}{V^{3/2}} = \frac{16\pi\epsilon_0}{9(-\alpha)^2} \cdot \sqrt{\frac{2e}{m}}\,\sin^2\left(\frac{\theta}{2}\right). \qquad (3.8)$$

This is the basic equation in the design of electron guns of spherical form.

Table 3.1. α as a function of $\bar{r}_c/\bar{r}_a$ [13].

$\bar{r}_c/\bar{r}_a$	$(-a)^2$	$(-a)^{4/3}$	da/dy	$\bar{r}_c/\bar{r}_a$	$(-a)^2$	$(-a)^{4/3}$	da/dy
1.00	0.0000	0.0000	1.0000	2.12	0.91729	0.94407	01.6060
1.01	0.0009996	0.00215	01.0059	2.15	0.96124	0.97399	01.6209
1.02	0.0039969	0.0054008	01.0119	2.17	0.99098	0.99398	01.6308
1.05	0.00245	0.01818	01.0298	2.20	1.0627	1.02404	01.6456
1.10	0.00962	0.04524	01.0592	2.25	1.1135	1.0743	01.6702
1.15	0.02127	0.07676	01.0884	2.30	1.1929	1.1248	01.6947
1.20	0.03716	0.11135	01.1172	2.35	1.2745	1.1755	01.7191
1.25	0.05710	0.14828	01.1457	2.40	1.3581	1.2264	01.7433
1.30	0.08091	0.18706	01.1739	2.45	1.4438	1.2774	01.7674
1.33	0.10842	0.22737	01.2019	2.50	1.5314	1.3286	01.7913
1.40	0.13949	0.26897	01.2296	2.60	1.7127	1.4315	01.8389
1.45	0.17399	0.31166	01.2571	2.70	1.9016	1.5349	01.8861
1.50	0.21178	0.35530	01.2843	2.80	2.0979	1.6388	01.9328
1.55	0.25276	0.39977	01.3114	2.90	2.3015	1.7432	01.9790
1.60	0.29682	0.44497	01.3382	3.00	2.5120	1.8479	02.0249
1.65	0.34386	0.49082	01.3648	3.20	2.9533	2.0584	02.1156
1.70	0.39380	0.53726	01.3912	3.50	3.6634	2.3764	02.2489
1.75	0.44655	0.58422	01.4174	3.70	4.1673	2.5896	02.3362
1.80	0.50202	0.63166	01.4434	4.00	4.9662	2.9108	02.4649
1.85	0.56016	0.67953	01.4692	4.50	6.4037	3.4492	02.6739
1.90	0.62089	0.72779	01.4949	5.00	7.9708	3.9903	02.8770
1.92	0.64589	0.74720	01.5051	6.00	11.46	5.0830	03.1678
1.95	0.68414	0.77642	01.5204	7.00	15.35	6.1157	03.6412
1.97	0.71013	0.79596	01.5306	10.00	29.19	9.4802	04.6814
2.00	0.74983	0.82537	01.5458	30.00	178.2	31.667	010.0745
2.02	0.77682	0.84504	01.5559	50.00	393.3	53.861	014.2229
2.05	0.81798	0.87464	01.5710	100.00	1144	109.380	—
2.07	0.84589	0.89442	01.5810	300.00	6031	331.324	—
2.10	0.88846	0.92418	01.5960	500.00	13015	553.294	—

3.2. The focusing electrode

The effect of the missing electrons around the conical sector of half angle θ is replaced by using a focusing electrode around the cathode. It is at the same potential as the cathode and of axially symmetrical form (Fig. 3.1.).

Analytical solution of the form of the focusing electrode is difficult but it has been done in closed form for axially symmetric flow between planes (Pierce-type gun [9,14,15]). The focusing electrode should maintain the potential distribution on the edge of the beam as in

the presence of space charge from the other electrons in the spherical diode to satisfy the requirements of Poisson's and of Laplace's equations.
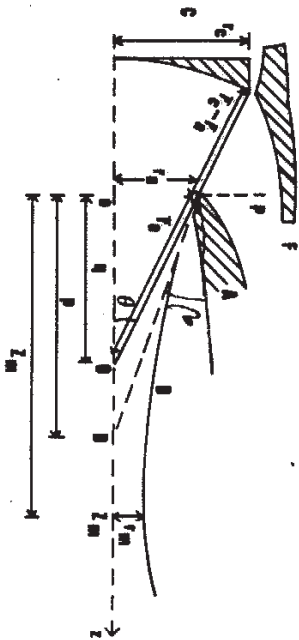
Figure 3.1. The spherical electron gun and definition of its dimensions. A = Anode, B = actual beam edge, C = cathode, O = the center of anode and cathode spheres, D = deflected focus, F = focusing electrode, P = cardinal plane of the anode lens.

There are also other analytical and numerical methods for solving the shape of the focusing electrode [16,17,18,19]. However, they are too complicated to be used in this work.

3.3. Effects of the anode aperture

Now we are in a position to choose the cone half-angle θ and fix the ratio $\bar{r}_a/\bar{r}_c$ using the Langmuir solution Eq. (3.8) for the desired perveance. However, as we will see later the random choice of θ does not necessarily result in good gun performance and desired optical quality. The main reason for this is the effect of the anode aperture because it acts as a divergent lens. This may cause variations in emissivity at cathode surface due to deviation of the potential distribution from ideal in the neighbourhood of the symmetry axis.

As a first approximation for the focal length of the anode lens we can use a formula by Davisson and Calbick [20,21]

$$f_{DC} = \frac{4V}{E_2 - E_1} \cdot \quad (3.9)$$

Here $E_2(=0)$ is the axial electric field behind the anode and E_1 is the axial field inside the gun. E_1 can easily be calculated from the expression of the potential

$$E_1 = \frac{4V}{3a} \frac{\frac{r}{a}}{\left(\frac{d\phi}{dy}\right)\frac{r}{a}} \quad (3.10)$$

and f_{DC} becomes

$$f_{DC} = -\frac{3a\,\frac{r}{a}}{\left(\frac{d\phi}{dy}\right)\frac{r}{a}} \cdot \quad (3.11)$$

Birdsall [22] has calculated a space charge correction for the focal length in the anode aperture leading approximately to 10 % reduction for perveance value $0,3 \cdot 10^{-6}$ (Pöschl and Veith [23]). This result is in fair accordance with the results of Brewer [24].

Kirstein and Hornsby [25] have developed an iterative solution method of Poisson's and Laplace's equations producing also electron trajectories. It consists of solving Poisson's equation in self-consistent manner and tracing the trajectories between the steps (see also the method of Amboss [26]).

Brewer [13] has shown graphically the experimental behaviour of the deflecting angle $\theta - \beta$ versus perveance, Fig. 3.2., compared with the value obtained according to Eqs. (3.11) and 3.12)

$$\theta - \beta = \arctan \sqrt{\frac{r_a}{f}} \cdot \quad (3.12)$$

From the experimental points shown in Fig. 3.2. one can calculate the real focal length and the ratio $\Gamma = f_{DC}/f_{corr}$ (Fig. 3.3).

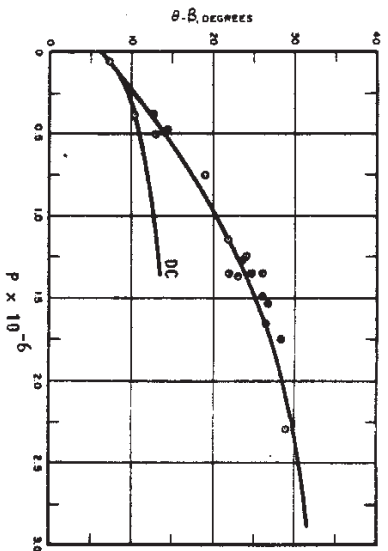For a good magnetic beam focusing the slope of the beam edge coming from the anode must obey [13]

Figure 3.2. Deflection of the beam edge behind the anode aperture, [13], ⊙ = experimental data, DC = Davisson-Calbick theory [20], [21].

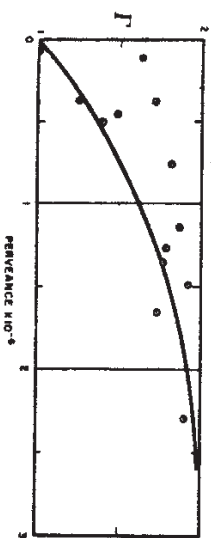Figure 3.3. Ratio of calculated to experimental focal length, ⊙ = experimental data, [13].

$$\frac{dr}{dz} \leq 0,4 \cdot \alpha \cdot \quad (3.13)$$

Thus the optimum cone half-angle of the gun can be calculated and fixed for chosen perveance

$$\theta_{opt} = (\theta - \beta) + 0,4 \cdot \alpha \quad (3.14)$$
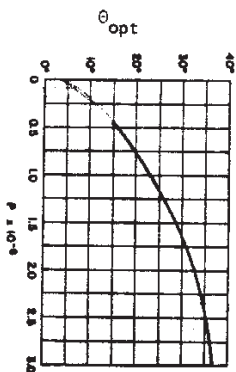
and this is shown in Fig. 3.4.

3.4. The cathode

The first phase in fixing the gun parameters is to determine the properties and dimensions of the cathode surface. For interchangeable cathodes, the lifetime of which does not have to be very long, pure tungsten suits best. Although it can be poisoned by some reactive gases it is not as sensitive for them as many other commonly used cathode materials. The most important limiting factor for the lifetime is the mass deposit from the cathode surface at high temperatures. This thins down the cathode wires or ribbons and after some loss of material (usually 12 %) the cathode will burn out.

In the present case the maximum ratings are: cathode current I_c = 0,3 A, anode voltage 10 kV and perveance $P = 0,3 \cdot 10^{-6}$. By choosing the maximum emission current density 3,5 A/cm² at temperature 2800 K we can calculate the characteristics of the cathode from the tables and graphs of von Ardenne [27]. His tables give for a cathode made of a ribbon of tungsten a thickness of 0,49 mm. The respective lifetime is about 210 h. We chose to use tungsten ribbon instead of wire or hairpin model due to the high cathode current.

The calculated effective surface area of the cathode was 8.6 mm² but we chose a slightly larger value 10,24 mm² to compensate for various losses caused by bending the edges of the ribbon and other deficiencies in its fabrication, Fig. 3.5.

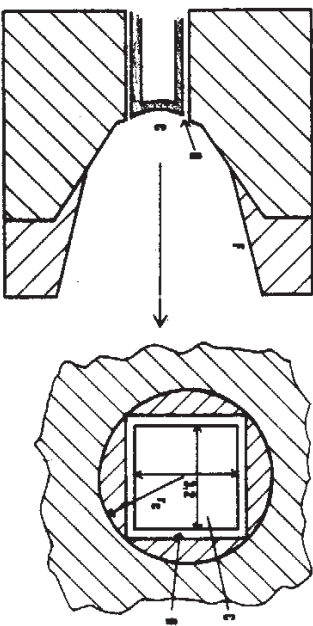Figure 3.4. The optimum convergence angle ([1]).

Figure 3.5. The ribbon cathode. The circular area around the cathode has the same radius of curvature as the cathode although it does not emit electrons. Dimensions are in mm. C = cathode, F = focusing electrode, G = gap = 0,1 mm, r_c = calculational radius = 3,0 mm.

To make easier the turning of the focusing electrode the circular area of radius r_c = 3,0 mm around the cathode had the same radius of curvature as the active cathode surface and this value for r_c was used in later calculations. It is obvious that this causes some effects on the optical and electrical properties of the gun but this decision was necessary for the laboratory workshop.

The form of the focusing electrode was found experimentally by varying the apex angles of the two cones (Fig. 3.5.) to obtain the desired optical and electrical quality for the gun. Usually this is done with the aid of an electrolytic tank or other analogous methods. It was, however, sufficient for present purposes to do this experimentally in a working gun prototype.

3.5. Gun parameters

The optimum angle of convergence, $\theta_{opt} = 13°$, for the gun can be read from Fig. 3.4. Since the radius of the cathode r_c is already fixed the radius of curvature of the cathode is now available for us from the geometry of the gun (Fig. 3.1.)

$$\bar{r}_c = \frac{r_c}{\sin\theta}, \qquad (3.15)$$

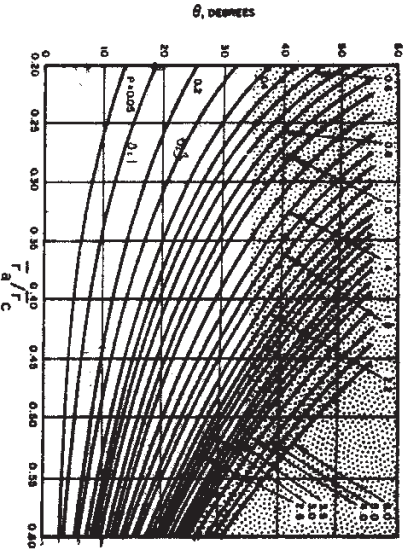$\bar{r}_a$ can be obtained from the solution of Langmuir and Blodgett, which is represented graphically in Fig. 3.6.

Figure 3.6. $\bar{r}_a/\bar{r}_c$ as a function of θ with the perveance as a parameter, [13].

The course of determination of gun parameters can be shown as in the flow chart in Fig. 3.7.

The values of r_m and z_m for the two different focal lengths were calculated employing equations (2.6) and (2.8). In the evaluation of (2.8) we used Simpson's rule obtaining quite sufficient accuracy. The determination of the behaviour of f_{DC} and f_{corr} as functions of perveance was done directly from Eq. (2.8) and the results of these
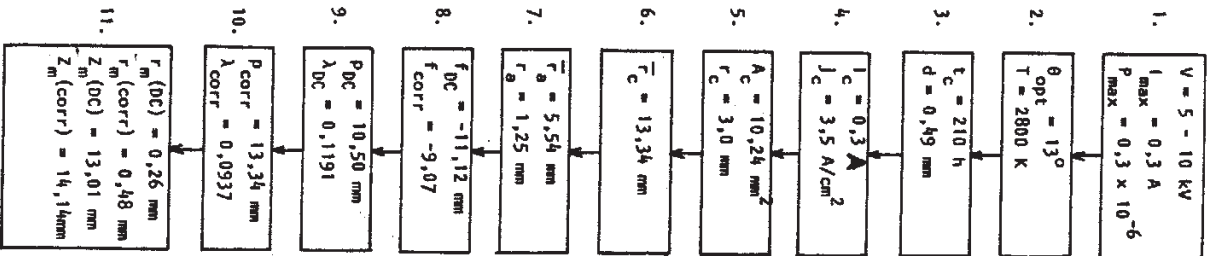
Figure 3.7. The determination of gun parameters.

1. $V = 5 - 10$ kV; $I_{max} = 0.3$ A; $P_{max} = 0.3 \times 10^{-6}$

2. $\theta_{opt} = 13°$; $T = 2800$ K

3. $t_c = 210$ h; $d = 0.49$ mm

4. $\frac{I_c}{J_c} = 0.3$; $J_c = 3.5$ A/cm²

5. $A_c = 10.24$ mm²; $r_c = 3.0$ mm

6. $\bar{r}_c = 13.34$ mm

7. $\bar{r}_a = 5.54$ mm; $r_a = 1.25$ mm

8. $f_{DC} = -11.12$ mm; $f_{corr} = -9.07$

9. $P_{DC} = 10.50$ mm; $\lambda_{DC} = 0.1191$

10. $P_{corr} = 13.34$ mm; $\lambda_{corr} = 0.0937$

11. $r_m(DC) = 0.26$ mm; $r_m(corr) = 0.48$ mm; $z_m(DC) = 13.01$ mm; $z_m(corr) = 14.14$ mm

1. $V = 5 - 10$ kV

2. θ_{opt} is obtained from Fig. 3.4.

3. See text. d = thickness of the cathode ribbon.

4. The maximum cathode current density J_c is defined by the maximum current I_c, cathode temperature and lifetime.

5. Cathode emissive area is defined by J_c and I. This gives the calculational r_c.

6. $\bar{r}_c$ comes from Eq. (3.15).

7. $\bar{r}_a$ is obtained from Fig. 3.6. and r_a from $\bar{r}_a - \bar{r}_a \sin\theta$.

8. f_{DC} is from Eq. (3.11) and f_{corr} is from Fig. 3.3.

9.&10. P_{DC} is the place of the tip of the deflected cone. It can be calculated using q, the distance of the original focus from the anode (see Fig. 3.1.) by the lens equation

$$P = \frac{qf}{q+f} \qquad (q<0) \qquad (3.16)$$

$$q = \frac{r_a}{\tan\theta}, \qquad (3.17)$$

λ_{DC} and λ_{corr} are the slopes of the beam edge for DC- and corrected theory. They are obtained from

$$\lambda = \frac{r_a}{P}. \qquad (3.18)$$

11. r_m and z_m are calculated by eqs. (2.6) and (2.8) respectively.

calculations are shown in Appendix D, where we also have $r_m = r_m(P)$ for both focal lengths.

In these calculations, of course, we suppose the geometry of the gun fixed and only the perveance is varied. Fig. C.1. in Appendix C shows that the point of minimum does not move very much as the perveance is changed. The range of the minimum point is about 3-4 mm and does not depend much on the chosen focal length. However, z_m varies rather strongly with f.

3.6. Effects of thermal velocities

The electrons emitted from the cathode surface have initial velocities distributed over all directions. In the electric field the electrons accelerate towards the anode. Thus the final velocity near the anode is a superimposition of the velocity gain in the field and the thermal velocity. Therefore the beam becomes somewhat diffuse. This naturally continues after the anode aperture throughout all the beam. The distribution of the current density is approximately Gaussian at the edges of the beam due to the fact that the electrons obey Boltzmann's velocity distribution when leaving the hot (T ≈ 2000 -3000 K) cathode.

Cutler and Hines [28] have calculated the effect of thermal velocities on the behaviour of the beam. They derived the standard deviation of the current density σ_{CH} at the beam edge for different gun geometries (Fig. 3.8).

Danielson et al. [29] have refined the calculations of σ and other gun properties taking into account the action of the anode lens which is, however, small. We use the results by Cutler and Hines in evaluating the beam spread. As a matter of fact, their σ_{CH} is not the standard deviation of the Gaussian (see their Eq. 3.?) and therefore the real σ must be read from the graphs of the current density profiles. Cutler and Hines have given the beam profile curves as a function of radius, Fig. 3.9..
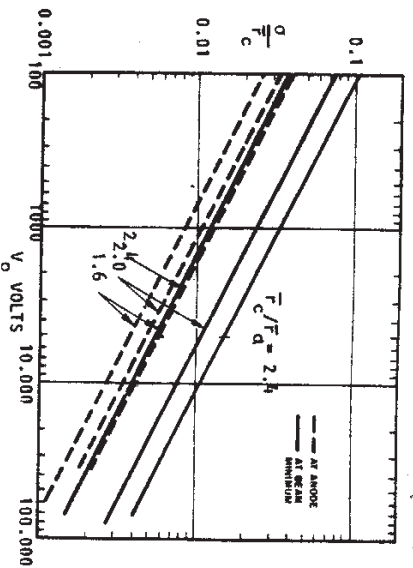
Figure 3.8. Standard deviation σ_{CH} for various gun geometries ([28], T = 1400 K, $\sigma \sim \sqrt{kT/V}$).
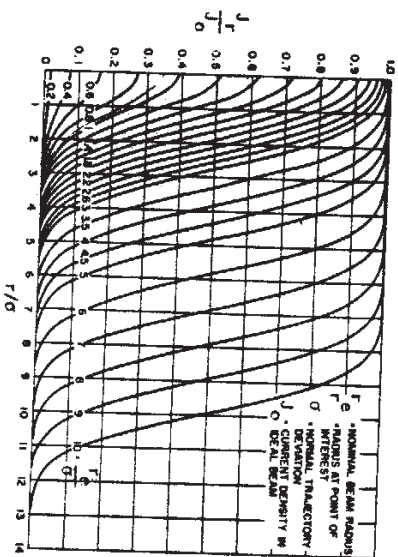

Figure 3.9. Thermally diffused current density of the electron beam, [28].

The standard deviation σ_{CH} can be read from Fig. 3.8., the values of which are given for the present example in table 3.2.

Table 3.2. σ_{CH} for two extreme voltages (T = 2800 K). σ_a at anode, σ_m at the beam minimum. r_{ea} and r_{em} are nominal beam radii and r_{em} is calculated using ref. [20,21]. Distances in millimeters.

V_a (kV)	σ_{mCH}	σ_{aCH}	r_{em}(DC)	r_{ea}
5	0.195	0.111	0.263	1.25
10	0.282	0.0774	0.263	1.25

The beam losses and the thermal load of the anode can be calculated approximately by defining the percentage of electrons outside a certain radius in the beam.

We can calculate the portion of electrons outside a given radius since in principle we know the standard deviation σ of the Gaussian. We suppose the beam current density to be of the form (Fig. 3.10).

$$J(r) = \begin{cases} e^{-\frac{(r-R)^2}{2\sigma^2}} & r \geq R \\ 1 & 0 < r < R \end{cases} \qquad (3.19)$$
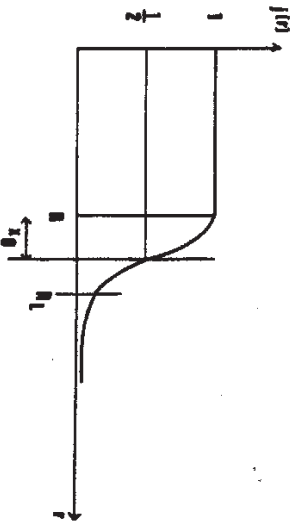
Figure 3.10. The assumed shape of the radial current density.

The standard deviation of the Gaussian σ becomes in this model in terms of the half-height width x_0

$$\sigma = \frac{x_0}{\sqrt{\ln 4}} , \qquad (3.20)$$

We define the amounts of electrons in different regions

$$I_I = \pi R^2, \qquad 0 < r < R, \qquad (3.21)$$

$$I_{II} = 2\pi \int_R^\infty dr\, r\, e^{-(r-R)^2/2\sigma^2} = $$
$$\pi\sigma[2\sigma + \sqrt{2\pi}\, R], \qquad r \geq R, \qquad (3.22)$$

Now we want to know the portion of electrons outside the arbitrary radius R_L ($\geq R$). Defining

$$I_{III} = 2\pi \int_{R_L}^\infty dr\, r\, e^{-(r-R)^2/2\sigma^2} = $$
$$2\pi\sigma^2 e^{-(R_L-R)^2/2\sigma^2} + \pi\sqrt{2\pi}\,\sigma R\, \text{erfc}\left(\frac{R_L-R}{\sqrt{2}\,\sigma}\right) \qquad (3.23)$$

the relative number of electrons outside R_L becomes

$$\frac{I_{III}}{I_I+I_{II}} = \frac{2\left(\frac{\sigma}{R}\right)^2 e^{-(R_L-R)^2/2\sigma^2} + \sqrt{2\pi}\left(\frac{\sigma}{R}\right)\text{erfc}\left(\frac{R_L-R}{\sqrt{2}\,\sigma}\right)}{1 + 2\left(\frac{\sigma}{R}\right)^2 + \sqrt{2\pi}\left(\frac{\sigma}{R}\right)} , \qquad (3.24)$$

This tells us the relative amount of the beam power dissipated at the anode with a hole of radius R_L (= r_a).

Now we evaluate the beam losses approximately employing equation (3.24) after drawing the current density profiles using Fig. 3.8.

They are shown in Fig. 3.11. and from these curves we define the radius R and the Gaussian deviation σ. We obtain for the anode dissipation the values given in table 3.3. For R_L we take three different values to exhibit the behaviour of the dissipation with varying anode aperture. The curves shown in Fig. 3.11. follow very well Gaussian distributions.
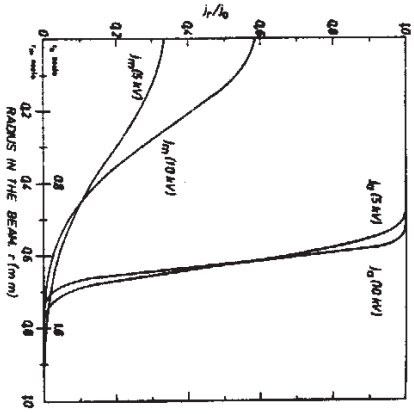

Figure 3.11. Current density distributions at the anode and the beam minimum (DC-model).

Table 3.3. Power losses of the gun. Gaussian standard deviations at anode are: V_a = 5 kV, $σ_a$ = 0.280 and V_a = 10 kV, $σ_a$ = 0.195. Dimensions are in millimetres.

V_a (kV)	R	R_L	loss n %	dissipation P_a (W)	P_a max (W)
5	0.920	1.25	14.1	75	530
5	0.920	1.30	10.6	56	530
5	0.920	1.40	5.6	30	530
10	1.020	1.25	9.7	292	3000
10	1.020	1.30	6.3	190	3000
10	1.020	1.40	2.3	69	3000

One of the most important characteristics of an electron gun is its

r_m, the radius of the beam at the minimum, in the presence of thermal spreading. The radius generally used include 95 % of the beam electrons. It can be immediately calculated from (3.24) for R = 0 and n = 5 %.

Since

$$n = e^{-R_L^2/2σ^2} ,\qquad (3.25)$$

where σ is the Gaussian standard deviation obtained directly from figure (3.11). Eq. (3.25) leads to

$$r_m(95) = σ\sqrt{2}\,\sqrt{-\log n} ,\qquad (3.26)$$

The values for r_m (95) are shown in table 3.4.

Table 3.4. Radius at the beam minimum including 95 % of beam electrons. Calculations are done according to the model by Davisson and Calbick [20,21]. Dimensions are

V_a (kV)	$σ_m$	r_m (95)
5	0.297	0.727
10	0.242	0.592

4. THEORY OF THE BEAM TRANSPORT SYSTEM

In this chapter we concentrate purely on magnetic focusing fields produced by axially symmetric coils or current distributions. Ironless coils lend themselves to simple calculations of axial fields needed in determination of electron-optical properties.

4.1. The field of a coil

To carry out electron optical calculations we need the axial field B_z of various coils. It is not difficult to calculate B_z for coils of rectangular cross section although we have to start from first principles since accurate formulas are not available. The magnetic induction is given by the law of Biot and Savart

$$\bar{B} = \frac{\mu_o I}{4\pi} \int \frac{d\bar{L} \times \bar{r}}{r^3} .$$ (4.1)

Applying Eq. (4.1) to an infinitesimal circular current loop of radius a at position z = ρ (Fig. 9.1.), B_z on z-axis becomes

$$B_z = \frac{I}{4\pi} \mu_o a^2 \int_0^{2\pi} \frac{d\phi}{r^3} = \frac{Ia^2 \mu_o}{2r^3} = \frac{Ia^2 \mu_o}{2(a^2 + (z - \zeta)^2)^{3/2}} ,$$ (4.2)

Thus the contribution of a single loop at z = ζ and R = -ρ is

$$dB_z = \frac{\mu_o IN}{2bc} \frac{(a + \rho)^2}{((a + \rho)^2 + (z - \zeta)^2)^{3/2}} d\rho d\zeta ,$$ (4.3)
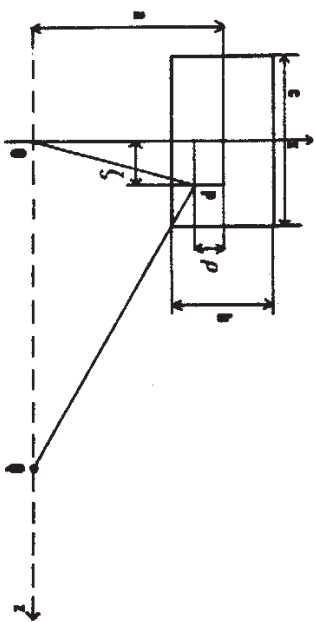
Figure 4.1. Definition of coil coordinates. $\overline{OP} = \bar{R}$, $\overline{PQ} = \bar{r}$, $d\bar{L} = dx\hat{i} + dy\hat{j}$, $\bar{r} = \bar{R} + z\hat{k} = R(\cos\phi\,\hat{i} + \sin\phi\,\hat{j}) + z\hat{k}$, $(d\bar{L} \times \bar{r})_z = -R^2 d\phi$.

Here IN/bc describes the current density of the element and N the number of turns of the coil. The axial field becomes

$$B_z = \frac{\mu_o IN}{2bc} \int_{-c/2}^{c/2} d\zeta \int_{-b/2}^{b/2} d\rho \frac{(a + \rho)^2}{((a + \rho)^2 + (z - \zeta)^2)^{3/2}}$$

$$= \frac{\mu_o IN}{2} R(z) ,$$ (4.4)

This can be integrated by substitution a + ρ = t and by changing the order of integration

$$R(z) = \frac{1}{bc} \left[(z + \frac{c}{2})\ln\left| \frac{a + \frac{b}{2} + \sqrt{(z - \frac{c}{2})^2 + (a + \frac{b}{2})^2}}{a - \frac{b}{2} + \sqrt{(z - \frac{c}{2})^2 + (a - \frac{b}{2})^2}} \right| \right.$$

$$\left. - (z - \frac{c}{2})\ln\left| \frac{a + \frac{b}{2} + \sqrt{(z + \frac{c}{2})^2 + (a + \frac{b}{2})^2}}{a - \frac{b}{2} + \sqrt{(z + \frac{c}{2})^2 + (a - \frac{b}{2})^2}} \right| \right] ,$$ (4.5)

This is an accurate solution and the familiar single loop approximations (Fert and Durandeau [30], Lyle [31] and Liebmann [32]) can be obtained from Eq. (4.5) by expanding the logarithms into power series up to second or third order.

4.2. Paraxial approximation

In this section we are going to study analytical and numerical methods of electron optics to obtain electron trajectories and focal lengths. The physical situation of an electron coming into the focusing magnetic field can (seen in Fig. 4.2.)
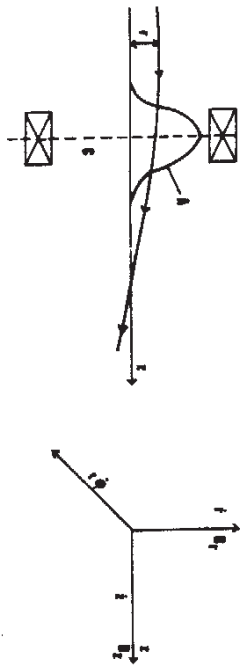
Figure 4.2. a) Electron trajectory in magnetic field and b) velocity coordinates. A = the axial field distribution, C = the cardinal plane, $v_r = \dot{r}, v_\phi = r\dot{\phi}, v_z = \dot{z}$.

In paraxial approximation (r small) we obtain for the field components

$$B_r = -\frac{r}{2}\frac{\partial B_z(r=0,z)}{\partial z}$$ (4.6)

From the conservation of magnetic flux through two plane surfaces at a distance dz from each other [33]. Known velocities v_r, v_z and v_ϕ (note: $B_\phi = 0$) yield the components of the Lorentz force

$$\bar{F} = -e\bar{v} \times \bar{B}$$ (4.7)

$$= -e\left[\hat{e}_r v_\phi B_z + \hat{e}_\phi(v_z B_r - v_r B_z) - \hat{e}_z v_\phi B_r\right],$$

Hence we obtain the equations of motion

$$m\ddot{r} = -eB_z r\dot{\phi} + mr\dot{\phi}^2,$$ (4.8)

$$\frac{d}{dt}(r^2\dot{\phi}) = err\dot{B}_z - erB_r\dot{z},$$ (4.9)

$$m\ddot{z} = -eB_r r\dot{\phi},$$ (4.10)

Substituting (4.6) for B_r in Eqs. (4.9) and (4.10) we obtain

$$m\ddot{z} = -\frac{e}{2}r^2\dot{\phi}\frac{\partial B_z}{\partial z},$$ (4.11)

$$\frac{d}{dt}(mr^2\dot{\phi}) = \frac{d}{dt}(\frac{er^2 B_z}{2}).$$ (4.12)

Eq. (4.12) is immediately integrated

$$mr^2\dot{\phi} = \frac{er^2 B_z}{2} + C,$$ (4.13)

The initial condition $\dot{\phi}(B=0) = 0$ forces $C = 0$

$$\dot{\phi} = \frac{eB_z}{2m},$$ (4.14)

Eq. (4.11) modifies into

$$\ddot{z} = -(\frac{e}{2m})^2 r^2 B_z \frac{\partial B_z}{\partial z},$$ (4.15)

In paraxial approximation this is of the second order in r and can be neglected. Thus we are left with

$$\ddot{r} = -\frac{re^2 B_z^2}{4m},$$ (4.16)

which shows the radial acceleration is always towards the axis. By using

$$\ddot{r} = \frac{\partial^2 r}{\partial z^2}(\frac{\partial z}{\partial t})^2,$$ (4.17)

the energy relation

$$eV = \frac{mv^2}{2},$$ (4.18)

and the approximation

$$v \approx v_z = \dot{z} = \sqrt{\frac{2eV}{m}}$$ (4.19)

we obtain

$$\frac{d^2 r}{dz^2} = -\frac{eB_z^2}{8mV}\, r .$$ (4.20)

Similarly for ϕ

$$\frac{d\phi}{dt} = \frac{\partial\phi}{\partial z}\frac{dz}{dt} = \frac{eB_z}{2m} ,$$ (4.21)

$$\frac{\partial\phi}{\partial z} = \sqrt{\frac{e}{8mV}}\, B_z ,$$ (4.22)

and the rotation angle becomes after integration

$$\phi(z) = \sqrt{\frac{e}{8mV}} \int_{z_0}^{z} B_z\, dz .$$ (4.23)

From (4.20) and (4.23) it becomes apparent that knowing B_z is sufficient to calculate the behaviour of the electron in axially symmetrical fields in paraxial approximation.

4.3. The focal length

Eq. (4.20) allows calculation of the focal length for thin lenses (Fig. 4.3.)
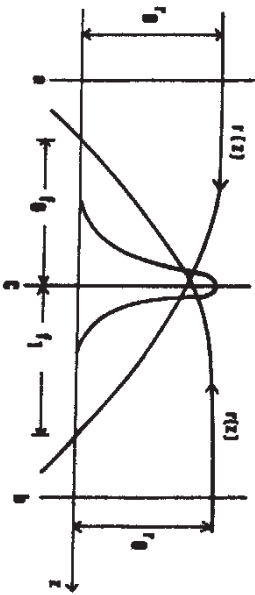
Figure 4.3. Definition of focal lengths f_0 and f_1. C is the cardinal plane.

Integrating Eq. (4.20) twice we obtain the electron trajectory [34]

$$r(z) = r_0 + \frac{e}{8mV} \int_a^z dt(t - z)\, B_z^2(t), \quad z \geq a .$$ (4.24)

The derivative of the trajectory is

$$r'(z) = -\frac{e}{8mV} \int_a^z dt\, B_z^2(t) .$$ (4.25)

Using the geometry (Fig. 4.3) we obtain approximately

$$f_1 r'(b) = r_0 \quad \text{(ray from left)},$$ (4.26)

$$f_0 r'(a) = -r_0 \quad \text{(ray from right)},$$ (4.27)

For thin symmetrical lenses $f_0 = -f_1$ and hence

$$f_0^{-1} = \frac{e}{8mV} \int_a^b dt\, B_z^2(t) = \frac{e\mu_0^2 I^2 N^2}{16mV} \int_{-\infty}^{\infty} R(z)^2\, dz ,$$ (4.28)

Writing this equation it is presumed the field is approximately zero at points a and b. This means for the ray entering from the left

$$r'(a) = 0$$ (4.29)

and from the right

$$r'(b) = 0 .$$ (4.30)

We apply for electron optics the corresponding optical equation for thin lenses, [30]

$$\frac{1}{p} + \frac{1}{q} = \frac{1}{f} ,$$ (4.31)

where p and q mean the distances of the image and object from the origin respectively.

As can be seen from Fig. 4.3. the approximations (4.26) and (4.27) are in fact crude causing large errors in cases when the lens fields are not thin. Since $\int R(z)dz$ is constant for the chosen coil geometry Eq. (4.28) results in an important proportionality

$$f = \frac{CV}{I_N^2} ,$$ (4.32)

To obtain a clear picture of electron motions in focusing magnetic fields an alternative method was used [35]. It is a simple numerical aid giving sufficient accuracy to trajectory calculations and to determination of focal lengths.

It is based on solving the electron trajectory equation in magnetic field in paraxial approximation (Eq. (4.20)).

$$r''(z) + \frac{eB^2(z)}{8mV} r(z) = 0$$ (4.33)

by a difference method. Taking Δz to be the length of the step we obtain

$$r_{n+1} = \left[2 - (\Delta z)^2 \frac{eB_0^2 R(zn)^2}{8mV} \right] r_n - r_{n-1} .$$ (4.34)

4.4. Design of the focusing lens

Computer calculations using Romberg method of integration were carried out to compute focal lengths from Eqs (4.5) and (4.28) with various coil geometries. These results showed clear deviations from preliminary trajectory calculations, where focal lengths were obtained by using lens equation (4.31). The focal length calculated from (4.28) turned out to be 30 % smaller than the one obtained from trajectory calculations

(a = 33 mm, b = 20 mm, c = 30 mm, N = 500, i = 2,6 A at V = 10 kV). The error diminishes as we approach large f or enlarge the radius a of the coil, (Fig. 4.4). It seems that for practical focal lengths (f about 20-30 mm) we must use the trajectory method. For weaker lenses (f ≳ 100 mm) it is sufficient to apply equation (4.28).

The trajectory method gives a reliable value for f since the beam (in fact its asymtote) obeys to a very good accuracy the lens equation. This fact can easily be verified from the figures to appear later in Appendix D.

In all these preliminary and later calculations the thermal spreading has been taken into account only in the initial values of the beam at its minimum behind the anode. This approximation was dictated by the complications caused by the simultaneous effects of the focusing field, space charge, and thermal transverse velocities. The focusing field causes some compensation for thermal spreading but for our purposes this can be neglected. The effects of space charge has been taken into account by calculating approximate asymptotes of electron trajectories in large-field regions, whereas in weak-field regions where magnetic force is negligible the trajectories have been calculated accurately.

In all calculations for the approximate radius of the beam edge was taken r(95). Since at the beam minimum the current distribution was taken a Gaussian, repulsive forces are stronger in the center of the beam, where the charge density is highest, than at the edge of the beam.

The focusing system consists of three successive identical ironless coils. The first two of them are placed to work with unit magnification whereas the third coil is placed to compress the emerging ray in desired ratio discussed in chapter 2.1.

To obtain a focal length approximately 30 mm the parameters of the coils were chosen: a = 33 mm, b = 20 mm, c = 30 mm, N = 500, i = 2,6 A (at V = 10 kV). The final focal length was calculated from the trajectories to be 29,5 mm.
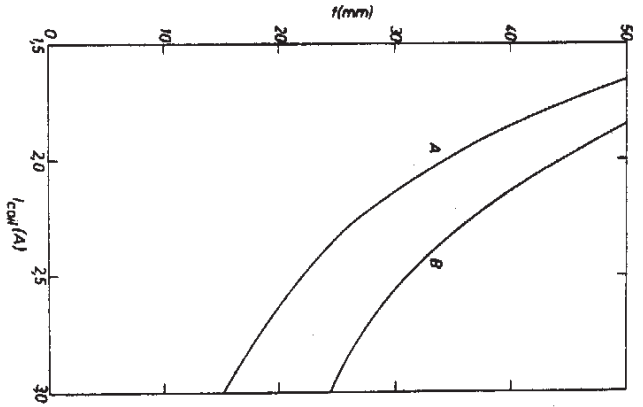
f(mm)

$I_{coil}(A)$

Figure 4.4. Focal lengths from trajectory calculations (A) and from Eq. 4.28 (B) as functions of coil current. Coil parameters: a = 33 mm, b = 20 mm, c = 30 mm, N = 500, I = 2,6 A (at V = 10 kV).

We explain first the case of 10 kV anode accelerating voltage at a perveance of P = 0,3 · 10^{-6} we assume to be constant in all subsequent calculations. The beam emerging from the gun diverges after the beam minimum (where r_m = 0,59 mm as we calculated earlier in DC-model) as shown in Fig. D.1. Appendix D. We have drawn an asymptote to represent the beam edge in the large field region, where the effect of the space charge is small.

The intersection of the asymptote and z-axis is equal to 2f from the center of the coil. The asymptotes have slopes λ and angles α as

shown in Appendix D. The distance of minimum r from the coil center was determined by forcing the asymptotic trajectories of space charge region and weak magnetic field region to coincide. Thus the total length of one coil system became 136 mm.

The image distance is equal to the object distance (= 2f = 59 mm) to obtain unit magnification. Fig. D.2. in Appendix D shows the corresponding beam edge trajectory exhibiting clearly the accuracy of the trajectory method used. For the first and second lenses the entrance and exit opening angles of the beam are equal. Fig. D.1. in Appendix D describes the space charge behaviour of the beam edge in all weak-field regions. The exit angle of the second coil is, naturally, equal to the entrance angle α_1 = 7,6° of the third coil. Now we want to obtain a beam having a linear compression $\kappa \approx 0,429$ with a minimum entrance diameter δ in a volume of length 10 mm in the sample gas chamber.

We know the slope of the asymptote of the entering beam edge in the third coil and obtain the emerging beam asymptote by first calculating the beam minimum radius r_m Eq. (2.6). This results to δ = 0,88 mm and r_m = 0,19 mm enabling one to draw the space charge curve in Fig. D.3. by Eq. (2.8) and to determine the slope of its asymptote.

Now we know both of the beam tangents in the third coil but we are still lacking the distances of object and image, q and p, Fig. 4.5. They can be solved as functions of the focal length f and the angles α_1 and α_2.

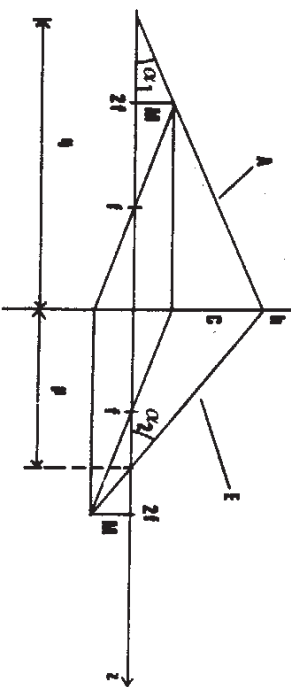Figure 4.5. Definition of optical terms. The asymptote of the entering (= A) and emerging (= B) beam edge. M = heights of virtual object and image, h = height of asymptote intercepts.

Assuming the lens thin and symmetrical and employing the geometry shown in Fig. 4.5., we obtain

$$\tan \alpha_1 = \frac{M}{q - 2f} ,$$

(4.35)

$$\tan \alpha_2 = \frac{M}{2f - q} = \frac{M}{h} ,$$

(4.36)

$$\frac{q - 2f}{q} = \frac{M}{h} ,$$

(4.37)

$$\frac{2f - p}{p} = \frac{M}{h} ,$$

(4.38)

From Eqs. (4.39) and (4.40) we solve p and q when f and the asymptotic angles are known.

Eqs. (4.35)-(4.38) result to ($\beta = \tan \alpha_2 / \tan \alpha_1$)

$$p = f(1 + \frac{1}{\beta}) ,$$

(4.39)

$$q = f(1 + \beta) .$$

(4.40)

The angle $\alpha_2 = 9.38°$ was determined graphically. Thus we obtain finally p = 66,1 mm and q = 53,3 mm. Fig. D.3. in Appendix D shows the space charge behaviour of the final beam edge together with its asymptote and Fig. D.4. in Appendix D the respective trajectory.

All these calculations can be repeated for the 5 kV case assuming that the coil distances are the same as for 10 kV. One exception from this procedure is, naturally, the determination of r_m in the sample chamber. This was done by fitting the beam edge asymptotes because in this case we do not know κ, but q, p and λ_1 instead, for the third lens.

Results from these calculations are shown in Figs. D.5.- 8 in Appendix D. Fig. 1.1. exhibits the dimensions of the final focusing system construction for 5 to 10 kV acceleration. The fact that the geometry of the focusing system remains approximately the same in this region of acceleration can be seen from the space charge behaviour of the beam Figs. D.1., 3., 5. and 8. In Appendix D, where the z-intercepts

of the asymptotes remain approximately the same for the two cases.

5. DISCUSSION

The final construction of the focusing system is exhibited in Fig. 1.1. It is not necessary to vary the coil positions as the potential is changed, only the coil current needs to be modified to keep the focal length constant.

The method used in trajectory calculations is quite suitable for this type of problems, where the magnetic field of the lens is known. The electron-optical calculations have been done assuming lossless beam advance and keeping the beam perveance constant. In practice there are losses of beam current in the apertures between the lenses and collisions to rest gas molecules. These are the main reasons for adjusting the coil positions. Also the thermal velocities of the electrons spread the beam and move the minima between the lenses further away. This has to be compensated for by moving slightly each of the coils.

On the other hand the rest gas ions neutralize the beam and tend to reduce the effect of space charge.

The choice of the focal length of the anode aperture affects strongly the location of the beam minimum. There seems to be some ambiguity concerning this matter. However, Miller [36] has pointed out that the Davisson - Calbick formula for focal lengths is a good approximation for cone half-angles up to 20°. By examining the graphs shown by Hechtel [16] we can see that for the chosen perveance $0,3 \cdot 10^{-6}$ and convergence angle 13° the anode aperture should cause only negligible errors to the electric field distribution on the cathode surface and thus to the current distribution. In our gun we use a square rather than circular cathode, and this necessarily causes unavoidable effects to the current distribution, r_m, z_m and the shape of the beam cross-section. These phenomena, if harmful for the optical quality of the gun, must be eliminated by experimentally

choosing the shape of the focusing electrode near the edge of the cathode.

6. REFERENCES

1. K. Siegbahn, L. Werme, B. Grennberg, J. Nordgren, C. Nordling, Phys. Lett. 41A, 111 (1972).

2. P. Pogrebnyak, Yu. Pavlenko, E. Verkhovtseva, Ya. Fogel', V. Udovenko, Instr. Exp. Techn. 17, 1481 (1974).

3. E. Verkhovtseva, V. Yaremenko, A. Ovechkin, Ya. Fogel, Opt. Spektrosk. 37, 221 (1974).

4. B. Henke, K. Taniguchi, J. Appl. Phys. 47, 1027 (1976).

5. K. Taniguchi, B. Henke, J. Chem. Phys. 64, 3021 (1976).

6. B. Henke, K. Taniguchi, Adv. X-Ray Anal. 19, 627 (1976).

7. I. Brytov, L. Mstibovskaya, L. Rabinovich, Izv. Akad. Nauk SSSR, Ser. Fiz. 40, 303 (1976).

8. J. Nordgren, H. Ågren, C. Nordling, K. Siegbahn, Ann. Acad. Reg. Scient. Upsaliensis 21, 23 (1978).

9. J. Pierce, Theory and Design of Electron Beams, van Nostrand, New York (1949).

10. R. Hutter, in Focusing of Charged Particles, Editor A. Septier, Academic Press, New York (1967), Vol. 2, p. 3.

11. H. Ivey, Adv. Electron. Electron Phys. 6, 138 (1954).

12. I. Langmuir, K. Blodgett, Phys. Rev. 24, 49 (1924).

13. G. Brewer, in ref. 10, p. 23.

14. J. Pierce, J. Appl. Phys. 11, 548 (1940).

15. J. Pierce, J. Appl. Phys. 15, 721 (1944).

16. R. Hechtel, Telefunken Ztg. 28, 222 (1955).

17. G. Brewer, J. Appl. Phys. 28, 634 (1957).

18. K. Harker, J. Appl. Phys. 31, 2165 (1960).

19. K. Harker, J. Appl. Phys. 33, 1861 (1962).

20. C. Davisson, C. Calbick, Phys. Rev. 38, 585 (1931).

21. C. Davisson, C. Calbick, Phys. Rev. 42, 580 (1932).

22. C. Birdsall, IRE Trans. Electron Devices 4, 132 (1957).

23. K. Püschl, W. Veith, Arch. Elektr. Übertragung 12, 45 (1958).

24. Ref. [13], p. 55.

25. P. Kirstein, J. Hornsby, IEEE Trans. Electron Devices 11, 196 (1964).

26. K. Amboss, J. Electron. Control 13, 545 (1962).

27. M. von Ardenne, Tabellen der Elektronenphysik, Ionenphysik und Übermikroskopie, VEB Deutsche Verlag der Wissenschaften Berlin (1956), Band I.

28. C. Cutler, M. Hines, Proc. IRE 43, 307 (1955).

29. W. Danielson, J. Rosenfeld, J. Saloom, Bell system Tech. J. 35, 375 (1956).

30. C. Fert, P. Durandeau In Focusing of Charged Particles, Editor A. Septier, Academic Press, New York (1967), Vol I P. 309.

31. T. Lyle. Phil. Mag. (6) 3, 310 (1902).

32. G. Liebmann, Proc. Phys. Soc. (London) B68, 737 (1955).

33. W. Glaser, Grundlagen der Elektronenoptik, Springer, Wien (1952) pp. 58, 86.

34. Ref. [33], p. 252.

35. P. Grivet, Electron Optics, Pergamon Press, Oxford (1965) p. 98.

36. H. Müller, Arch. Elektr. Übertragung 2, 20 (1955).

APPENDIX A. Space charge limited beam confined into a tube.
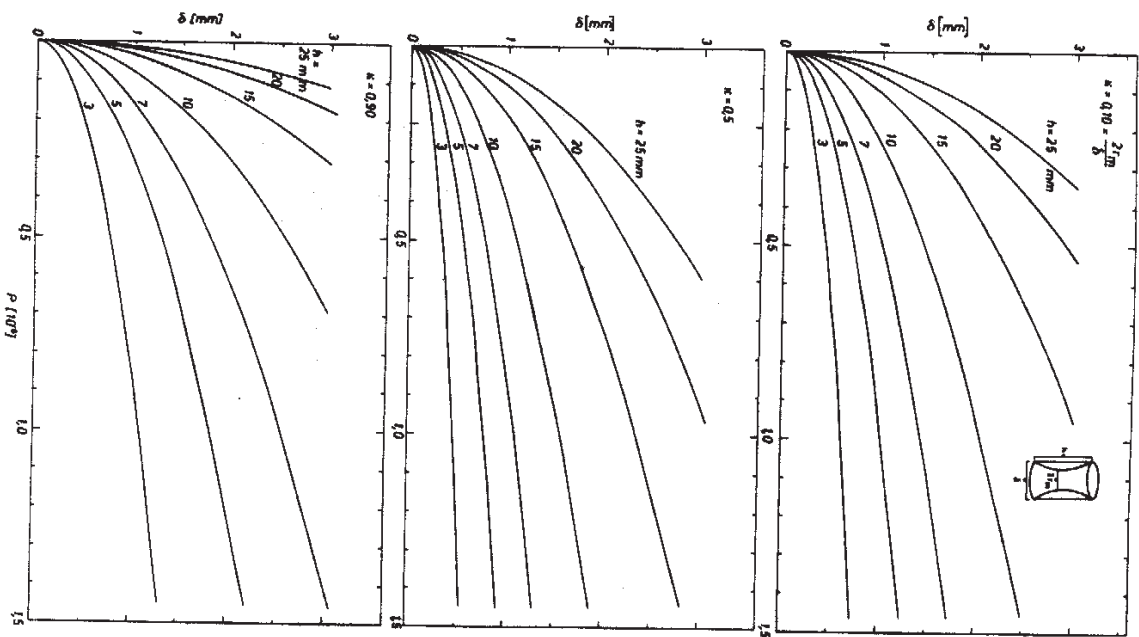
APPENDIX B. The Intensity on diffraction grating emitted from a ribbon source through a slit as a function of distance of the source from the slit. Slit dimensions δ = 0,05 mm, h = 10 mm. The height of the grating S = 12,5 mm.

Fig. B.1. The distance of the grating L = 206 mm and the angle φ = 1°59' with the source width M as a parameter.
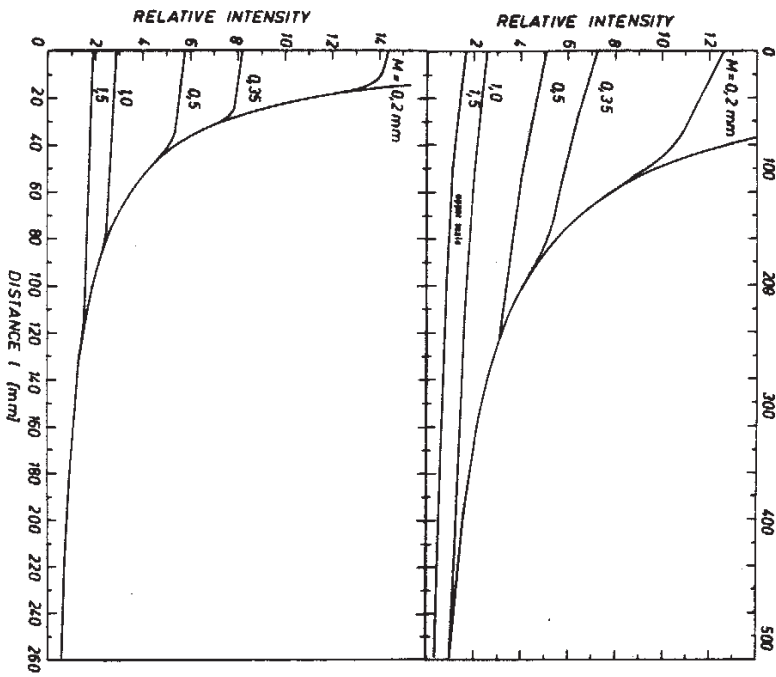
Fig. B.2. As Fig. B.1., L = 545 mm, φ = 15°49'.
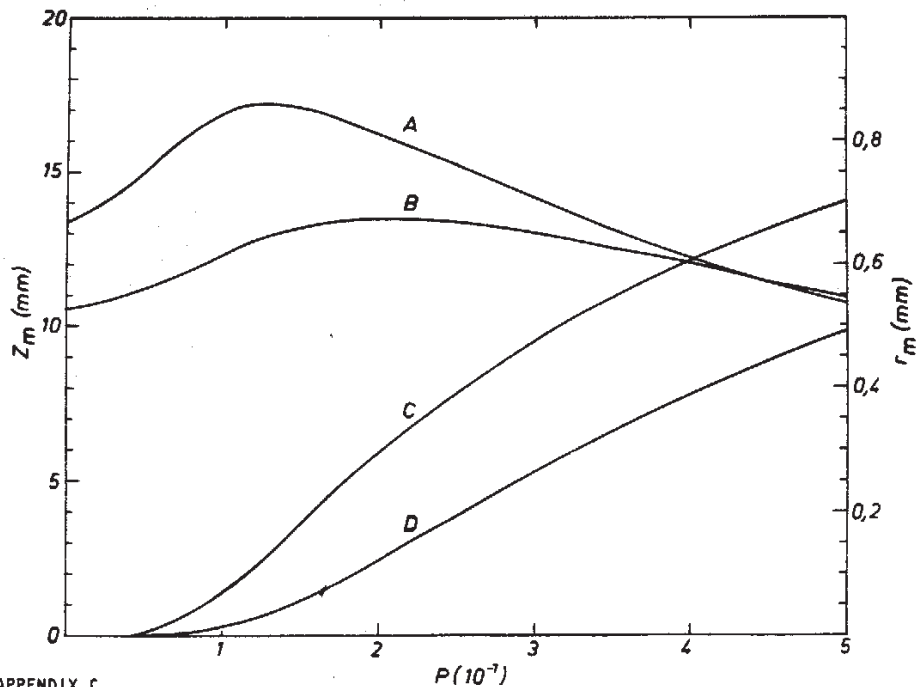
APPENDIX C.

Figure C.1. r_m and Z_m as functions of perveance for fixed gun geometry. r_m and Z_m include no thermal spreading. Gun parameters: P = 0,3 × 10^{-6}, θ = 13°, $\bar{r}_c$ = 13,34 mm, r_a = 5,54 mm. A and B = Z_m calculated with f_{corr} and f_{DC}, respectively. C and D = r_m calculated with f_{corr} and f_{DC}, respectively. f_{DC} = -11,12 mm, f_{corr} = -9,07 mm (see text).
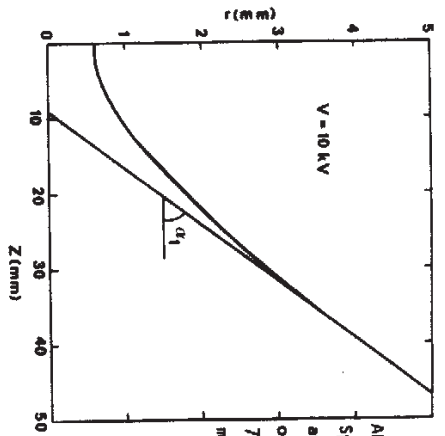
APPENDIX D. Figure D.1. Spreading of the beam behind the anode, r(95). r_m=0,59 mm, slope of the asymptote λ_1=0,1332, α_1= 7,59°; the origin is at the minimum of the beam.
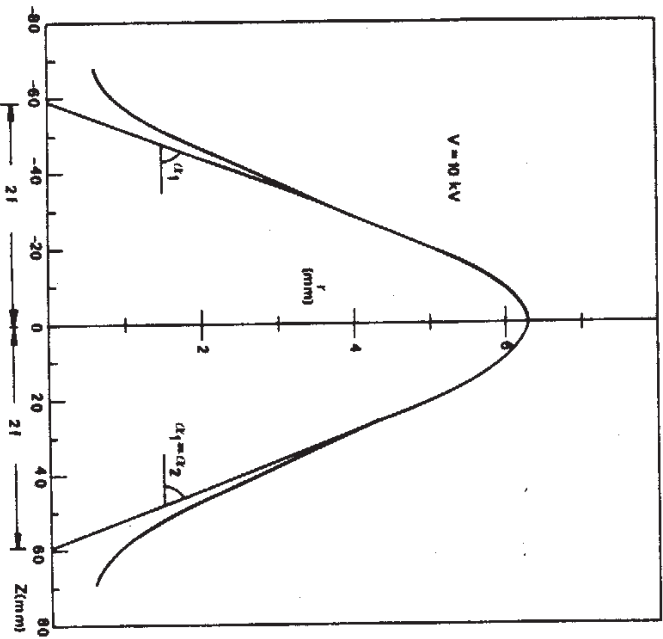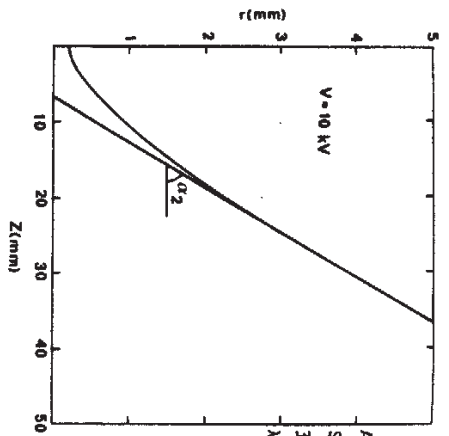
V = 10 kV

Figure D.2. Beam edge trajectory and its asymptotes for the 1st and 2nd lenses. Parameters are as in Fig. D.1. 2f = 59 mm.

V = 10 kV

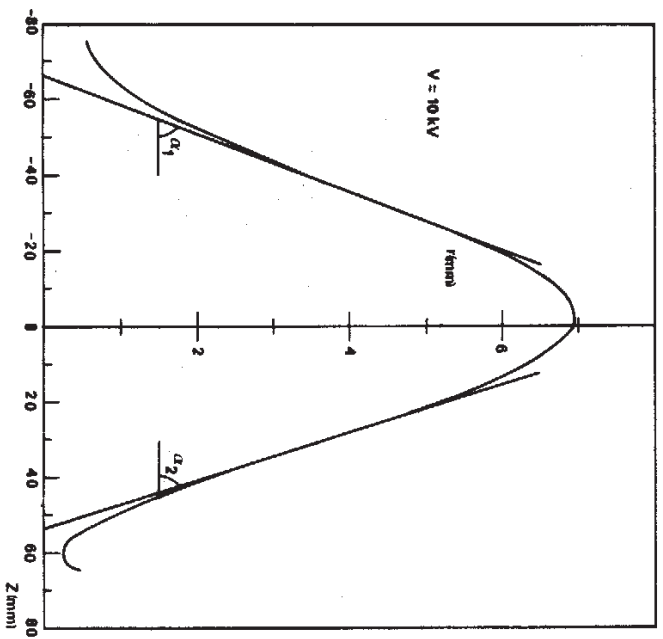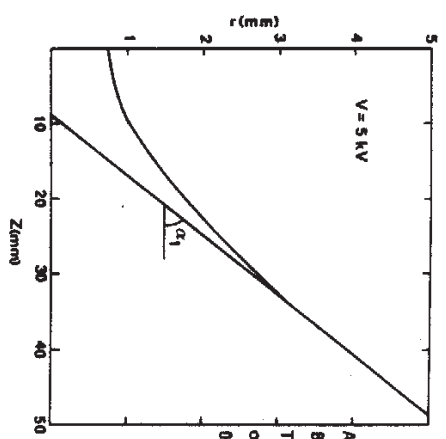APPENDIX D. Figure D.3. Spreading of the beam behind the 3rd lens. Parameters: r_m=0,19 mm, λ_2=0,1652, α_2=9,38°,

V = 10 kV

Figure D.4. Beam edge trajectory and its asymptotes for the 3rd lens. Parameters are as in Fig. D.3.

V = 10 kV

APPENDIX D. Figure D.5.
Beam spreading behind the gun.
The origin is at the minimum
of the beam. Parameters: $r_m =$
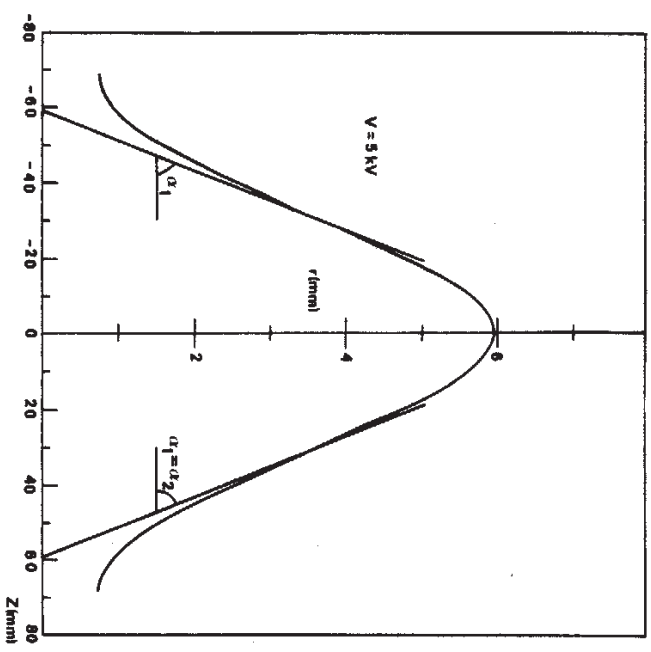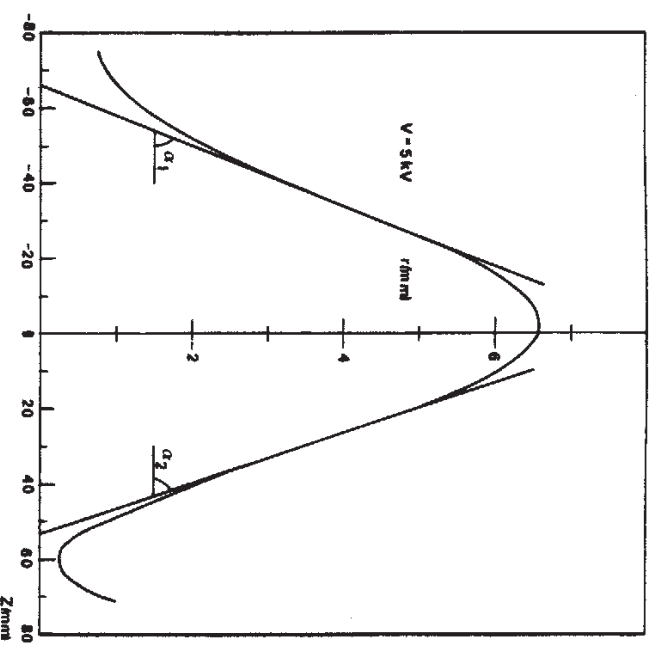0,73 mm, $\lambda_1 = 0,1260$, $\alpha_1 = 7,18°$.

Figure D.6. Beam edge trajectory and its asymptotes for the 1st and
2nd lenses. Parameters are as in Fig. D.5.

APPENDIX D. Figure D.7.
Beam edge trajectory and its
asymptotes for the 3rd lens.
Parameters: $r_m = 0,73$ mm, $\lambda_1 =$
0,1260, $\alpha_1 = 7,18$, $\lambda_2 = 0,1520$,
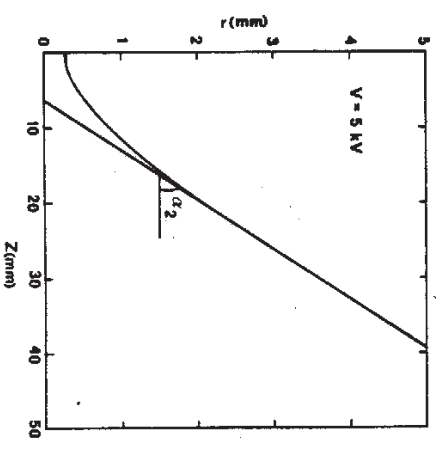$\alpha_2 = 8,64°$, $r_{m2} = 0,250$ mm.

Figure D.8. Beam spreading behind the 3rd lens. The slope of the
asymptote is fitted to λ_2 in Fig. D.7.